EPJ manuscript No.
(will be inserted by the editor)

Localization of eigenvectors in random graphs

František Slanina[1a]

Institute of Physics, Academy of Sciences of the Czech Republic, Na Slovance 2, CZ-18221 Praha, Czech Republic

the date of receipt and acceptance should be inserted later

Abstract. Using exact numerical diagonalization, we investigate localization in two classes of random matrices corresponding to random graphs. The first class comprises the adjacency matrices of Erdős-Rényi (ER) random graphs. The second one corresponds to random cubic graphs, with Gaussian random variables on the diagonal. We establish the position of the mobility edge, applying the finite-size analysis of the inverse participation ratio. The fraction of localized states is rather small on the ER graphs and decreases when the average degree increases. On the contrary, on cubic graphs the fraction of localized states is large and tends to 1 when the strength of the disorder increases, implying that for sufficiently strong disorder all states are localized. The distribution of the inverse participation ratio in localized phase has finite width when the system size tends to infinity and exhibits complicated multi-peak structure. We also confirm that the statistics of level spacings is Poissonian in the localized regime, while for extended states it corresponds to the Gaussian orthogonal ensemble.

PACS. 05.40.-a Fluctuation phenomena, random processes, noise, and Brownian motion – 89.75.-k Complex systems – 63.50.Lm Glasses and amorphous solids

arXiv:1401.1681v1 [cond-mat.stat-mech] 8 Jan 2014

1 Introduction

After more than 50 years, Anderson localization [1] remains one of the most puzzling problems of theoretical physics [2]. Although many results have been accumulated [3,4,5], open questions remain even in the very basic issue of the definition of the proper criterion of localization (as a single example, see e.g. [6]). From our viewpoint, however subjective it might be, we can classify the approaches to the phenomenon of localization into three big groups. In this introductory sketch we shall emphasize the results concerning Bethe lattices, as they are directly related to our work.

First, "physical" theories aim at grasping the essence without necessarily reaching the mathematical rigor. A typical examples are the scaling theory [7], the self-consistent theory [8,9,10], the approach based on parquet diagrams [11] and the approaches based on replica [12] and supersymmetry [13] methods. For our work, the relevant sources are the results concerning localization on Bethe lattice [14,15,16,17,18,19,20], where the exact self-consistent equation was formulated and the localization threshold was computed. The phase diagram exhibits extended states in the regime of weak disorder and energies sufficiently close to the band center. Otherwise the states are localized. There is a well defined mobility edge, separating extended states on one side from the localized states on the other side. Although in principle we cannot exclude mixed regimes [21], in which localized and extended states would coexist arbitrarily close to each other within a finite interval, such a mixed regime was not yet observed.

Second, "mathematical" theories prove rigorously the localization properties, but are limited to a few models where the known methods of proof work. Still, there is a good deal of results available now, see e. g. [22]. The result relevant for us is the proof of localization in the Bethe lattice [21,23]. However, the rigorous approaches work directly with infinite systems, thus avoiding the difficulties in taking the thermodynamic limit. On the other hand, it is the behavior of the system with increasing size that is physically most interesting. Hence, the physical interpretation of the rigorous results remains the matter of debate.

Third, one may resort to purely numerical computations, see e. g. [24] for electron localization or [25] for localization of acoustic waves. More sophisticated approaches rely on the cavity approximation (which becomes exact on trees) and numerical solution of thus obtained equation [26,27,28,29,30,31,32].

The results on the localization in Bethe lattices bring the problem close to the field of spectral theory [33] of random graphs [34], as many models of random graphs are locally tree-like. Therefore, all local properties of such random graphs should tend to Bethe lattice in thermodynamic limit. Mathematically, spectra of random graphs are the same thing as spectra of random sparse matrices. The latter were studied in depth using various methods [35,36,37,38,39,40,41,42,29,43]. Localization of eigenvectors was found both by exact numerical diagonalization [44,45,46,26,40,31] and using the cavity method [27,28,29,30].

[a] e-mail: slanina@fzu.cz

Here the study of random matrices touches again the problem of localization on a Bethe lattice, as we mentioned above.

Besides the academic interest in the localization phenomenon, numerous examples of practical application of the ideas of localization can be denonstrated, mainly in the area of complex networks [47,48,49,50] or in the field of the analysis of biological [51] and social networks [52,53].

We quoted several times the results showing the presence of localization threshold for disordered Hamiltonians on Bethe lattices. The fact is now confirmed by rigorous mathematic methods, as well as physical arguments and numerical work on finite samples. However, several problems remain. First, it is not quite clear how the rigorous mathematic results should be translated to the reality of physical experiments. Second, the Bethe lattice is pathological from many points of view. Indeed, strictly speaking, in numerical studies we work with a Cayley tree, rather than Bethe lattice. The difference resides in the boundary conditions. In the Cayley tree the volume of "surface" sites is comparable to "bulk" sites, while the negligibility of the former is the basis for the existence of basic physical quantities, like the free-energy density. In the present work we shall try to avoid the problem of surface by working with random graphs. Our approach is based on the belief that in thermodynamic limit the Bethe lattice and random graph results coincide. For a mathematical justification, see [54].

In our previous work [55] we showed that the cavity approach, which may be considered as an approximation, coincides with the replica approach, which is assumed to be exact, in thermodynamic limit. The variational formalism introduced in [55] enables us to consistently formulate approximations.

The present work is a continuation of that of Ref. [55]. First, we show how the formalism of [55] can be extended to study localization. The equations found are in principle exact, but as soon as we resort to approximations developed and used in Ref. [55], we find that these approximations are insufficient to capture localization. Therefore, in the rest of the study we resort to exact numerical diagonalization followed by finite-size scaling analysis.

2 Cavity equations for localization

Among the diverse criteria of localization, the most suitable for our purposes is the behavior of the inverse participation ratio (IPR). Let L be a $N\times N$ real symmetric matrix with eigenvalues λ_i, $i=1,\ldots,N$ and corresponding normalized eigenvectors $e_{j\lambda_i}$. We shall assume implicitly, that the matrix elements of L are random variables with properties described later. The resolvent will be denoted $R(\zeta)=(\zeta-L)^{-1}$ and its diagonal element $g_i(\zeta)=R_{ii}(\zeta)$ for $\zeta\in\mathbb{C}\backslash\{\lambda_i; i=1,\ldots,N\}$. The IPR at $\lambda=\lambda_i$ for some i is

$$\begin{aligned} q^{-1}(\lambda) &= \sum_j e_{j\lambda}^4 = \\ &= \lim_{\varepsilon\to 0^+} \frac{\varepsilon\sum_i g_i(\lambda+\mathrm{i}\varepsilon)\, g_i(\lambda-\mathrm{i}\varepsilon)}{\mathrm{Im}\sum_i g_i(\lambda+\mathrm{i}\varepsilon)} \,. \end{aligned} \tag{1}$$

For the proof of the latter equality, see [56,30]. The definition (1) applies for fixed system size N. On the other hand, the question we ask in the analysis of localization is, whether the states within a certain interval, $\lambda\in I$, remain localized when $N\to\infty$ for all typical realizations of the disorder. Therefore, we should define more properly the average IPR in the interval I as

$$\langle q_I^{-1}\rangle = \left\langle \frac{1}{N_I}\sum_{i:\lambda_i\in I}\sum_j e_{j\lambda_i}^4 \right\rangle \tag{2}$$

where $\langle\ldots\rangle$ means averaging over the realizations of L and $N_I=\sum_{i:\lambda_i\in I}1$ is the number of eigenvalues within the interval I. Then, if we find that $\langle q_I^{-1}\rangle\to 0$ as $N\to\infty$, the states in I will be considered extended, while non-zero limit would imply localization of at least some of the states in the interval I. We shall assume that the extended states, if they exist, are found around the center of the spectrum, while localized states, if any, should be expected at the upper and lower tails. More complicated cases will not be treated here. The mobility edges are then defined as numbers $z_{\mathrm{mob}}^-<z_{\mathrm{mob}}^+$ such that

$$\lim_{N\to\infty}\langle q_I^{-1}\rangle \quad \begin{cases} = 0 & \text{for any } \ I\subset[z_{\mathrm{mob}}^-, z_{\mathrm{mob}}^+] \\ > 0 & \text{for any } \ I\subset(-\infty, z_{\mathrm{mob}}^-) \\ & \quad\text{or } I\subset(z_{\mathrm{mob}}^+,\infty)\,. \end{cases} \tag{3}$$

Let us now sketch the formalism using the cavity method. It consists in neglecting loops, so that it becomes exact on Bethe lattice, or on any tree in general. We denote $g(\zeta)$ the diagonal element of the resolvent at the root of the tree. Following [55] we introduce the generating functions

$$\begin{aligned} \gamma(\omega) &= \left\langle e^{-\omega\, g(\zeta)}-1\right\rangle \\ \Gamma(\omega,\omega') &= \left\langle \left(e^{-\omega\, g(\zeta)}-1\right)\left(e^{-\omega'\, g(\zeta')}-1\right)\right\rangle \,. \end{aligned} \tag{4}$$

The dependence on ζ and ζ' is assumed implicitly. We can extract the linear and bilinear terms from the generating functions as $\gamma(\omega)=\omega\left(s_1(\zeta)+O(\omega)\right)$ and $\Gamma(\omega,\omega')=\omega\omega'\left(s_2(\zeta,\zeta')+O(\omega,\omega')\right)$. Hence we deduce the expression for the average IPR in the limit $N\to\infty$

$$q^{-1}(z)|_{N\to\infty} = \lim_{\varepsilon\to 0^+}\frac{\varepsilon\, s_2(z+\mathrm{i}\varepsilon, z-\mathrm{i}\varepsilon)}{\mathrm{Im}\; s_1(z+\mathrm{i}\varepsilon)} \,. \tag{5}$$

Strictly speaking, the expression (5) is incorrect for two reasons. First, the order of the limits $\varepsilon\to 0^+$ and $N\to\infty$ is reversed, because the cavity approach works effectively with infinite N from the very beginning. Second, in (5)

the average over disorder is performed separately in the numerator and in the denominator, while if done properly, the averaging must involve the fraction as a whole. Without entering into deep discussions, we assume that neither of the two "mistakes" induce a fundamental fault into the results. To support this assumption we can note, first, that also Refs. [30,57] rely on the harmless exchange of the order of limits. Second, as for the independent averaging of the numerator and denominator, it is justified if we suppose that $g_i(\lambda+\mathrm{i}\varepsilon)$ is a self-averaging quantity, because in that case the disorder-average of the denominator is safely replaced by the sum $1/N\sum_i \bullet$.

If the degrees of the random graph are Poisson distributed, as is the case for the Erdős-Rényi random graph, with average μ, we obtain, for the one-particle generating function $\gamma(\omega)$ a self-consistent equation in the form

$$\begin{aligned}\gamma(\omega) &= \sqrt{\omega}\int_0^\infty \frac{d\lambda}{\sqrt{\lambda}}\, I_1(2\sqrt{\omega\lambda})\,\rho(\lambda)\\ \rho(\omega) &= e^{-\omega z+\mu\,\gamma(\omega)}\ .\end{aligned} \tag{6}$$

At this level, introduction of the auxiliary function $\rho(\omega)$ seems arbitrary, but it acquires clear sense in the variational approach developed in [55].

For calculating IPR, the two-particle quantities are needed. Without repeating the steps which lead to (6), we can write the equation for $\Gamma(\omega,\omega')$ as

$$\begin{aligned}\Gamma(\omega,\omega') \;=\; &\sqrt{\omega\omega'}\int_0^\infty \frac{d\lambda}{\sqrt{\lambda}}\int_0^\infty \frac{d\lambda'}{\sqrt{\lambda'}}\times\\ &\times\; I_1(2\sqrt{\omega\lambda})\, I_1(2\sqrt{\omega'\lambda'})\,\rho(\lambda)\,\rho(\lambda')\times\\ &\times\; e^{\mu\,\Gamma(\lambda,\lambda')}\ .\end{aligned} \tag{7}$$

Solving (6) and (7) should in principle give full description of the localization phenomenon. Note that the formalism used in [14] and [28] should be a special case of ours. Indeed, Refs. [14,28] work with the joint probability density for real and imaginary part of $g(z+\mathrm{i}\varepsilon)$, which is equivalent to the joint generating function for $g(z+\mathrm{i}\varepsilon)$ and $g(z-\mathrm{i}\varepsilon)$.

Full solution of (6) and (7) is not yet known. Approximative schemes for solving (6) were shown in [55], partially repeating the older results of [40,42]. The simpler one of the approximations used in [55] is the effective-medium approximation (EMA), which can be formulated as an ansatz $\rho(\omega) = e^{\omega\,\sigma(\zeta)}$. For $\sigma(\zeta)$ we find the cubic equation

$$\sigma^3 - \zeta\,\sigma^2 + (\mu-1)\,\sigma + \zeta = 0\ . \tag{8}$$

The density of states is non-zero only within the interval $[z_-, z_+]$ where $\mathrm{Im}\,\sigma(z+\mathrm{i}\varepsilon)$ is non-zero in the limit $\varepsilon\to 0^+$. Therefore, EMA exhibits sharp band edges, which is wrong, because the true spectrum contains Lifschitz tails extending arbitrarily far. Nevertheless, it is instructive to try to use EMA as a starting point for approximative solution of the equation (7). We insert in (7) the functions $\rho(\lambda)$, $\rho(\lambda')$, containing $\sigma(\zeta)$ obtained by solving (8). Still, the resulting integral equation for Γ is not readily soluble, so we apply further approximation, leaving only the lowest (bilinear) term in the expansion of $\Gamma(\omega,\omega')$ and expanding $e^{\mu\Gamma}$ on the right-hand side into series. This way we obtain an equation for s_2 and the solution is then supplied into (5). The IPR is then expressed through the function $\sigma(z)$ for $z\in\mathbb{R}$. Finally we get

$$q^{-1}(z) = \frac{\big(3\sigma^2(z) - 2z\sigma(z) + \mu - 1\big)\sigma^4(z)}{\big(\sigma^2(z)-1\big)\big(\sigma^4(z)-\mu\big)} \tag{9}$$

for $z\in\mathbb{R}\backslash[z_-,z_+]$ and $q^{-1}(z)=0$ for $z\in[z_-,z_+]$. The result is shown in Fig. 1 for $\mu=3$. We shall see later that this expression reflects qualitatively well the behavior of IPR at the tails of the spectrum. However, the result (9) is rather illusory, because localization indicated by non-zero IPR occurs only in the areas where density of states is strictly zero. The mobility edge coincides with the band edge. Therefore, the fraction of localized states is zero within such an approximation. We can try to improve the result applying the single-shell approximation (SSA) introduced in [55]. Within this approximation, we obtain for σ the equation

$$z^2 = \mu + z\sigma + e^{-\mu}\sum_{l=1}^{\infty}\frac{\mu^l}{(l-1)!}\,\frac{l}{z\sigma - l}\ . \tag{10}$$

As for the density of states in the Lifschitz tail, SSA does give some improvement, although severe artifacts of the approximation remain, namely the spurious band gaps inside the Lifschitz tail. (See Fig. 5 and [55] for details.) In the same way as in EMA, we can take the function $\sigma(\zeta)$ obtained in SSA, insert it into (7) and expand $\Gamma(\omega,\omega')$ into series. Thus, we obtain

$$\begin{aligned}q^{-1}(z) = &\left(\frac{2}{1-e^{-\mu}\sum_{l=1}^{\infty}\frac{\mu^l}{(l-1)!}\,\frac{l}{(z\sigma-l)^2}} - \frac{\sigma}{z}\right)^{-1}\times\\ &\times\,\frac{\sigma^4(z)}{\sigma^4(z)-\mu}\ .\end{aligned} \tag{11}$$

The result is shown in Fig. 2. Contrary to EMA, the dependence of the inverse participation ratio on eigenvalue is not monotonous, and the "interruptions", where $q^{-1}(z)=0$ occur exactly at the intervals where the density of states is non-zero. Therefore, SSA suffers from the same flaw as EMA, that is the IPR is non-zero only if density of states is zero. The conclusion of this section is that analytical solution of (7) would require more sophisticated methods than those at our disposal.

In the rest of this work, we will rely on exact numerical diagonalization results. However, the position of the band edge, as found in EMA, will serve as a benchmark for the position of the mobility edge and will be compared with numerical results.

3 Localization in Erdős-Rényi graphs

The first model we shall investigate is the adjacency matrix L of the Erdős-Rényi random graph. Apart from the

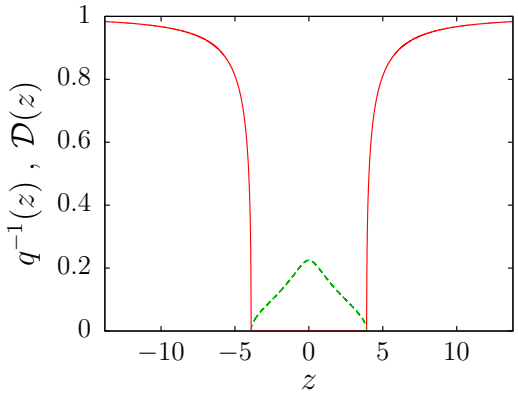

Fig. 1. Inverse participation ratio (solid line) and density of states (dashed line) calculated using the effective medium approximation, for Erdős-Rényi graph with average degree μ=3.

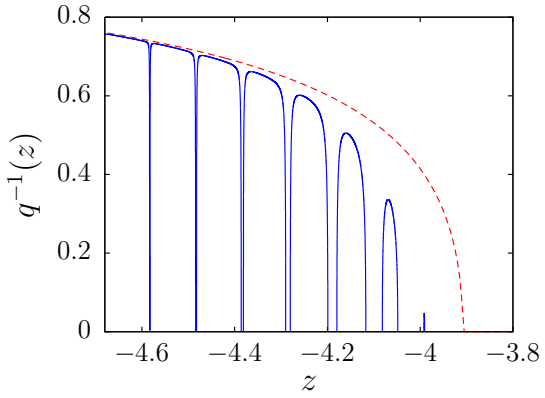

Fig. 2. Inverse participation ratio, for Erdős-Rényi graph with average degree μ=3 calculated using the effective medium approximation (dashed line) and single-shell approximation (solid line).

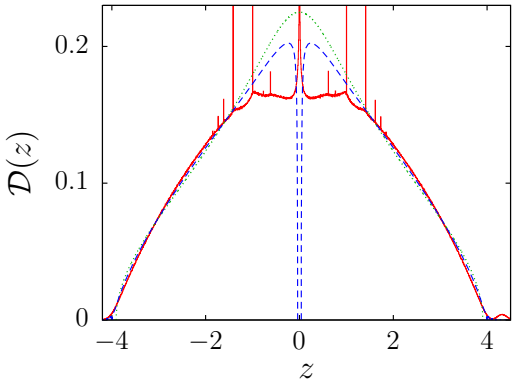

Fig. 3. The density of states for the adjacency matrix of the ER graph with $\mu = 3$, $N = 1000$, averaged over 115000 realizations (full line). For comparison, approximate results using EMA (dotted) and single-shell approximation of [55] (dashed) are shown.

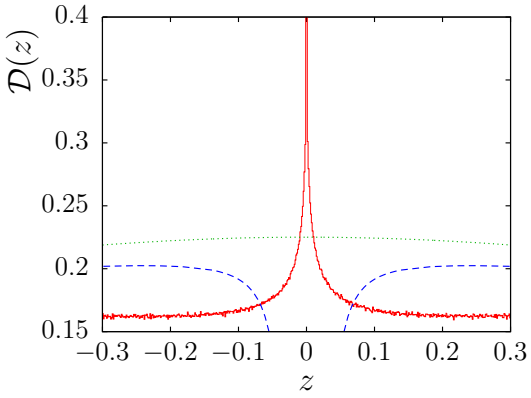

Fig. 4. Detail of the data of Fig. 3, showing the singularity at $z = 0$.

fact that L is symmetric matrix with zero on the diagonal, the matrix elements are independent and equally distributed. The probability density for a single off-diagonal element is

$$\pi_1(x) = \Big(1 - \frac{\mu}{N}\Big)\delta(x) + \frac{\mu}{N}\delta(x-1)\ . \qquad (12)$$

We investigated in depth the spectrum of L in [55]. In Fig. 3 we reproduce one of the results. The density of states has a very complicated structure, with many singularities and δ-function components. For example, an acute, perhaps logarithmic, singularity resides at the center of the spectrum, at $z = 0$, as shown in Fig. 4. The theory exposed in Ref. [41] could in principle bring an explanation of that singularity, bud we did not perform the calculations in this direction.

It is interesting to compare such suppression of localization in ER graphs with the localization which occurs in weakly diluted systems, where the localization is enhanced instead, by the mechanism of maximum entropy walk [58]. Indeed, on irregular graphs, for example the common ER graph or a regular graph with a few edges removed, the standard random walk does not posses maximum entropy. The requirement of entropy maximization introduces a non-local constraint, which, rather unexpectedly, favors localization.

At the tails of the spectrum, there is no sharp band edge, but a Lifschitz tail develops. The asymptotic form of the Lifschitz tail is now well established [35,42,55] and our numerical results can be seen in Fig. 5.

It is just the Lifschitz tail where the localization is expected. To have a first glance on that, we plot the IPR averaged over several tens of thousand realizations. In Figs 6 and 7 we show the results for $N = 1000$ and for $\mu = 3$ and $\mu = 5$, respectively. Comparing the behavior of IPR with the density of states, as shown in Fig. 3, we observe the same complicated structure of singularities. Generally, IPR is large at the tails, as well as close to the singularities in the density of states. One would naively expect that localization would occur in all regions where IPR is large, but it is true only in the tails. As we stressed earlier, we must check the behavior of IPR when N grows. Close to the singularities, we found IPR large, but consistently decreasing with increasing system size. On the contrary, lo-

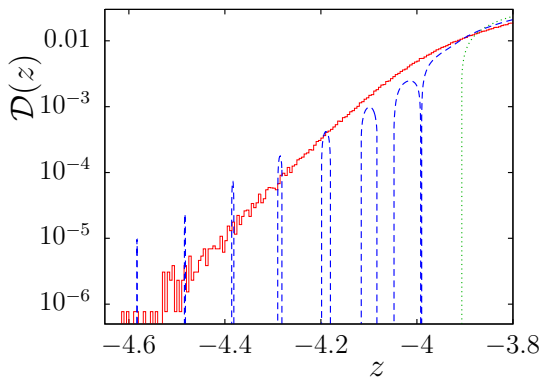

Fig. 5. Lower tail of the data of Fig. 3. Note that the single-shell approximation is superior to EMA in the Lifschitz-tail region, but still it is far from satisfactory.

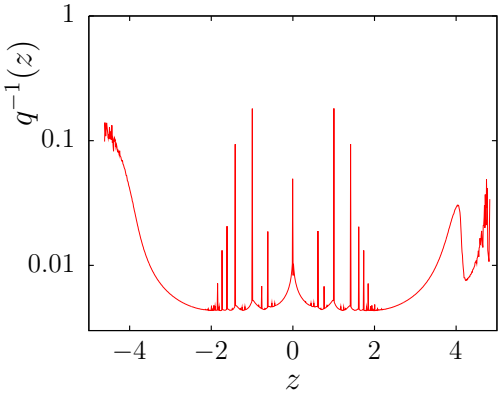

Fig. 6. Inverse participation ratio averaged over 115000 realizations, for ER graph with $\mu = 3$ and $N = 1000$.

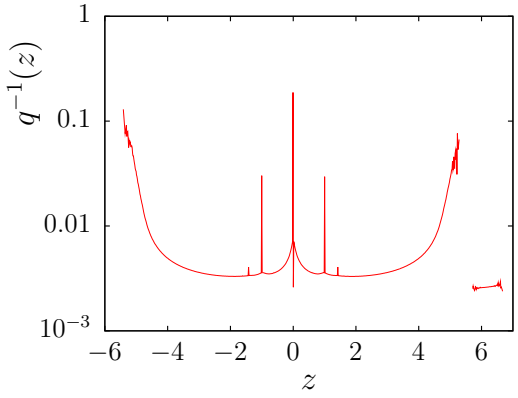

Fig. 7. Inverse participation ratio averaged over 65000 realizations, for ER graph with $\mu = 5$ and $N = 1000$.

calization in Lifschitz tails is clearly visible, as indicated in Figs 8 and 9. In the following, we decided to work with the lower tail, because the upper tail is somewhat obscured by the single maximum eigenvalue which behaves differently than all the rest of the spectrum. We can see that below certain value of z, the IPR is independent of N, within the range of statistical errors, while above this value, IPR decreases with N. We identify this value with the mobility edge. We shall describe the method of extracting the mobility edge from the data in the next section. Here we make only a few observations.

First, this definition of mobility edge is practical but it is not the only possible. Moreover, there might be even some doubts of it. Indeed, above the mobility edge the IPR should not only decrease with N, but decrease in a specific manner, namely as $1/N$, otherwise the states cannot be considered properly extended. Therefore, the alternative definition of the mobility edge would be as follows. We declare the states in the interval I extended, if $\langle q_I^{-1} \rangle \sim N^{-1}$ for $N \to \infty$, otherwise the states are considered localized. The data from Figs 8 and 9 indicate that the mobility edge defined in the latter way would lie somewhat higher than in the former. The difference may well be just a finite-size effect, but we cannot exclude also the possibility that it reflects a real phenomenon, namely presence of states which are neither properly extended, nor exponentially localized. For example, the eigenvectors can be characterized by tails decreasing slower than any exponential, but on the level of knowledge provided by our numerical data this is a mere speculation. However, note that eigenvectors with power-law tails do occur in certain models [59,60] and an interval of coexistence of extended and localized states was also hypothesized in [21]. In all the rest we shall stick to the former definition of the mobility edge for purely practical reasons.

Second, comparing the IPR calculated using EMA and SSA, shown in Fig. 2 with numerical findings in Figs 8 and 9 , we observe a qualitative agreement. On the other hand, quantitatively, EMA and SSA give much too high values of IPR. So, however defective EMA and SSA are with respect to localization, they do provide a hint of how IPR should behave.

Third, the data suggest that IPR for infinite system approaches a non-zero limit when we approach the mobility edge from the localized side. Because in extended regime IPR is strictly zero for infinite system, IPR should exhibit a discontinuity at the mobility edge. This confirms results obtained earlier in [61] using supersymmetric method.

Let us continue with the analysis of our results. Having established the mobility edge, we want to know how it depends on the average degree of the ER graph. This dependence is shown in Fig. 10. For comparison, we show also the position of the band edge, as found in EMA. We can see that the mobility edge is slightly below the EMA band edge, but the two quantities share a common trend. Therefore, the EMA band edge can serve as a useful zeroth approximation for the line of separation between localized and extended states. This criterion was used, without further justification, in the context of diffusion models for biological evolution [62].

In order to see quantitatively, how much globally relevant is the localization phenomenon, we measure the fraction of eigenvalues below the mobility edge

$$f_{\mathrm{loc}} = \left\langle \frac{1}{N} \sum_{i:\lambda_i < z_{\mathrm{mob}}^-} 1 \right\rangle . \qquad (13)$$

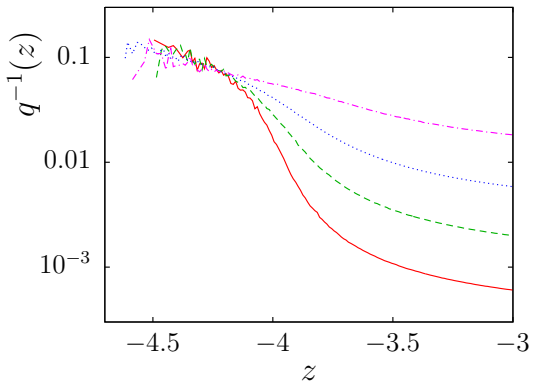

Fig. 8. Inverse participation ratio at the lower tail of the spectrum for ER graph with $\mu = 3$. The system size is $N = 10^4$ (solid line), 3000 (dashed line), 1000 (dotted line), and 300 (dash-dotted line). The data are averaged over 900, 10000, 65000 and 130000 realizations, respectively.

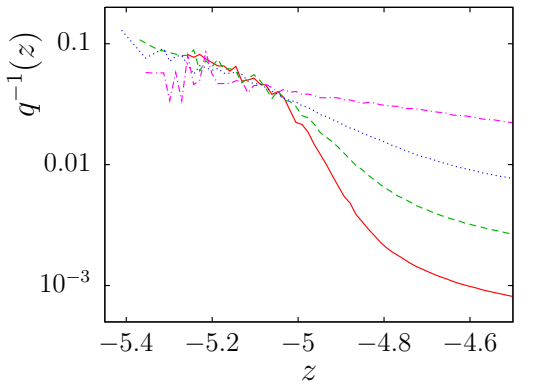

Fig. 9. Inverse participation ratio at the lower tail of the spectrum for ER graph with $\mu = 5$. The system size is $N = 10^4$ (solid line), 3000 (dashed line), 1000 (dotted line), and 300 (dash-dotted line). The data are averaged over 800, 5000, 65000 and 50000 realizations, respectively.

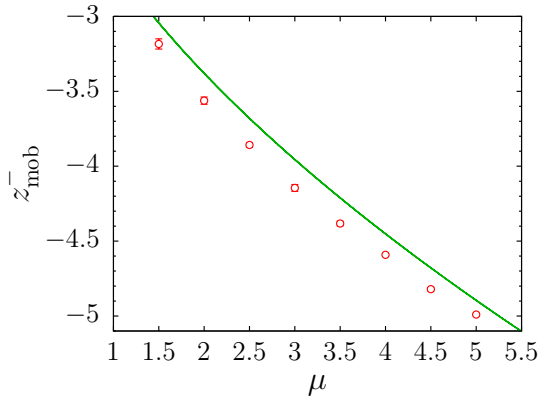

Fig. 10. Position of the mobility edge at the lower tail of the spectrum, for ER graph. Where not shown, error bars are smaller than the symbol size. The solid line is the band edge calculated in EMA.

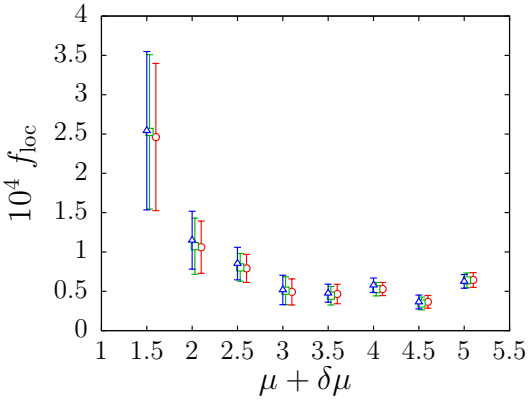

Fig. 11. Fraction of states below the lower mobility edge, for ER graph. We compare the results for $N = 10000$ (triangles), 3000 (squares), and 1000 (circles). For better visibility, the points are slightly shifted rightwards by $\delta\mu = 0$, 0.03, and 0.1 for $N = 10000$, 3000, and 1000, respectively.

Supposing that the spectrum is mirror-symmetric, as it should be in the limit $N \to \infty$, the total fraction of localized states is $2f_{\rm loc}$. We can see the results in Fig. 11. The first thing to note is that the results are practically independent of system size, so we can safely claim that they represent the fraction of localized eigenvalues for infinite system. The fraction decays with average degree μ, until it saturates around $\mu \simeq 3$ at a value close to $f_{\rm loc} \simeq 0.5 \cdot 10^{-4}$. It is suposed that this fraction should drop to zero in the limit $N \to \infty$, because it is known that all states are extended in an ER graph, on condition that $\mu \to \infty$ simultaneously with $N \to \infty$ [63]. The numerical procedure does not enable us to work with large enough N to see that explicitly. Therefore, we consider the saturation a finite-size effect.

4 Localization in random cubic graphs

4.1 Diagonal disorder

The second family of graphs investigated here are the random cubic graphs, i. e. random graphs satisfying the only constraint that the degree of all vertices is equal to 3. We decided to study this family as a kind of direct opposite of the ER graph. In ER graph, the properties are mostly due to inhomogeneity in the degrees. In cubic graph all degrees are equal. In ER graph, there is no diagonal disorder. In cubic graph, the relevant disorder is only on the diagonal. Of course, one can study also models which interpolate the two extremes, but we shall not do that in the present work. We shall rather compare the differences between the extremes.

The off-diagonal elements of the matrix L to study are identical to the adjacency matrix of the graph, while diagonal elements of L are independent Gaussian random

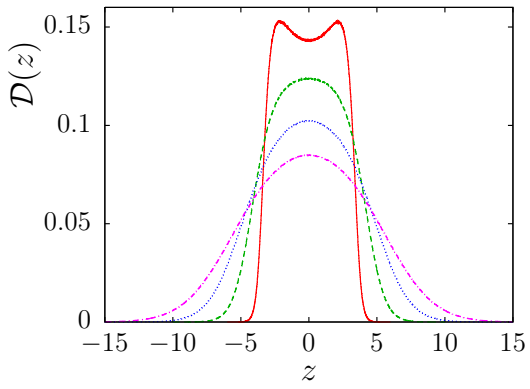

Fig. 12. Density of states for random cubic graph with diagonal disorder, for $N = 1000$. The disorder strength is $\eta = 1$ (solid line), 2 (dashed line), 3 (dotted line), and 4 (dash-dotted line). The data are averaged over 40000 realizations.

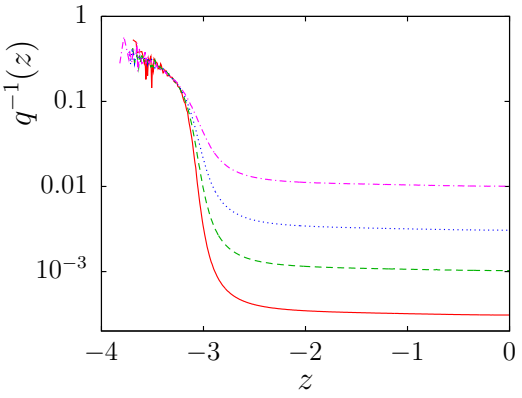

Fig. 13. Inverse participation ratio at the lower tail of the spectrum for random cubic graph with disorder strength $\eta = 0.5$. The system size is $N = 10^4$ (solid line), 3000 (dashed line), 1000 (dotted line), and 300 (dash-dotted line). The data are averaged over 550, 11000, 65000, and 160000 realizations, respectively.

variables, with probability density

$$\pi_{\mathrm{diag}}(L_{ii}) = \frac{1}{\sqrt{2\pi}\,\eta} \exp\left(-\frac{L_{ii}^2}{2\eta^2}\right) \tag{14}$$

In thermodynamic limit the local topology of the graph is identical to the Bethe lattice with coordination number 3 and the randomness of the structure, i. e. the off-diagonal disorder, must be irrelevant, as long as we investigate local properties of the graph and its size goes to infinity. For example, the density of states for the random graph with $\eta = 0$ must approach a non-random function identical to the well-known density of states of the Bethe lattice

$$\mathcal{D}_{\mathrm{Bethe}}(z) = \frac{3}{2\pi} \frac{\sqrt{8 - z^2}}{9 - z^2} \,. \tag{15}$$

The non-trivial ingredient is the randomness in diagonal elements of the matrix L and this is the feature which leads to localization here. The situation is somewhat complementary to the ER case investigated in the last section. In ER graphs, localization is due to off-diagonal disorder, while here the diagonal disorder is responsible.

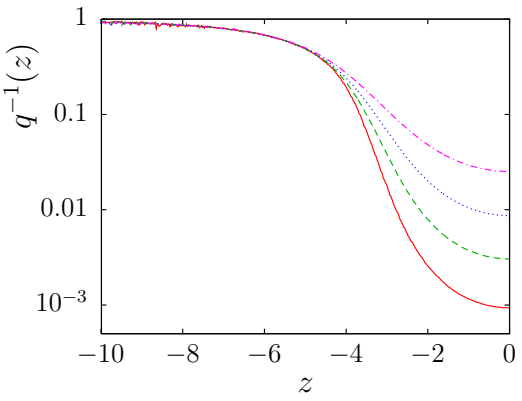

Fig. 14. Inverse participation ratio at the lower tail of the spectrum for random cubic graph with disorder strength $\eta = 2$. The system size is $N = 10^4$ (solid line), 3000 (dashed line), 1000 (dotted line), and 300 (dash-dotted line). The data are averaged over 610, 10000, 65000, and 160000 realizations, respectively.

4.2 Mobility edge

We show in Fig. 12 the density of states for several disorder strengths. The density of states is smooth and free of singularities, which are typical of the spectrum of ER graphs. The localized states occur in the Lifschitz tails, as we can clearly see in Figs. 13, 14, and 15. Qualitatively, we observe that localization is much stronger than in ER graphs and the IPR reaches values very close to 1. On the other hand, establishing the mobility edge is more difficult, because the deviations of the curves for different N are much smaller and obscured by statistical noise. We illustrate it in the inset of Fig. 15. In such a situation it is necessary to develop a method for extracting the mobility edge as reliably as possible. The method is illustrated in Fig. 16. The procedure we used consists in comparing the difference of average IPR for two system sizes, $\Delta q^{-1} = q^{-1}(N) - q^{-1}(N')$ with the level of statistical noise δq^{-1}. The estimate for the mobility edge $z^-_{\mathrm{mob}}(N, N')$ is found where the difference Δq^{-1} as a function of z crosses the noise level δq^{-1}. The error produced in this method is estimated in a similar manner, as difference of points where $\Delta q^{-1}(N, N')$ crosses δq^{-1} and where it crosses twice as large noise $2\delta q^{-1}$. The error bars shown if Figs. 10 and 17 are obtained in this way. We found that the estimate $z^-_{\mathrm{mob}}(N, N')$ depends quite strongly on the sizes N, N'. Therefore, we further extrapolate the values found to infinite system, as shown in the inset of Fig. 16.

The dependence of the mobility edge on disorder strength is shown in Fig. 17. As in the case of ER graphs, we compare the dependence of the mobility edge on disorder strength with the position of the band edge calculated using the effective medium approximation. While in ER

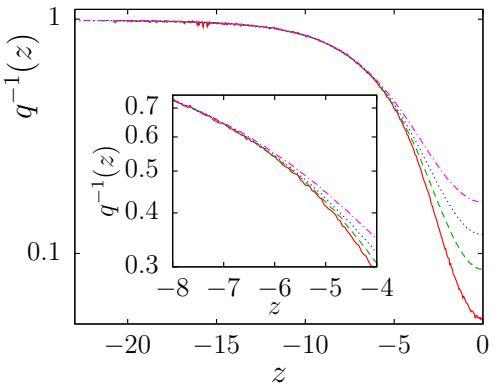

Fig. 15. Inverse participation ratio at the lower tail of the spectrum for random cubic graph with disorder strength $\eta = 4$. The system size is $N = 10^4$ (solid line), 3000 (dashed line), 1000 (dotted line), and 300 (dash-dotted line). The data are averaged over 550, 10000, 65000, and 160000 realizations, respectively. In the inset, detail of the data illustrating the difficulty to establish the mobility edge precisely.

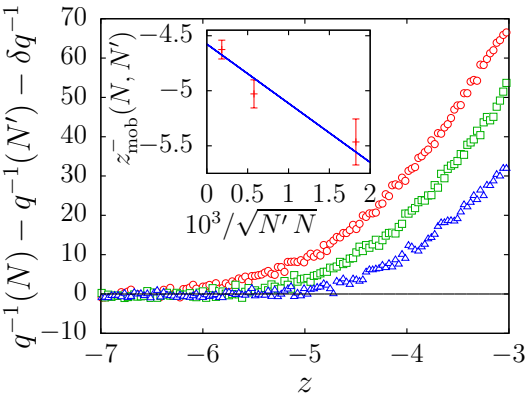

Fig. 16. An example of the procedure for establishing the mobility edge. The symbols correspond to the pairs of sizes $N = 300$, $N' = 1000$ (circles); $N = 1000$, $N' = 3000$ (squares); $N = 3000$, $N' = 10000$ (triangles). The estimated mobility edge for this pair is located where the data fall below zero. In the inset, extrapolation of the estimated mobility edge to infinite system size.

graph the EMA band edge and the mobility edge go in parallel, in random cubic graph they behave differently. While the EMA band edge grows in absolute value, thus reflecting the overall broadening of the density of states for increasing disorder, the mobility edge remains deep within the range of the EMA band. For disorder stronger than about $\eta \simeq 4$ the interval of extended states starts narrowing. This agrees qualitatively with earlier results on Anderson localization on Bethe lattice [15,23] which state that for strong enough disorder, $\eta > \eta_c$, all states are localized. Note that the same qualitative behavior was also found by diagrammatic methods for lattices in large Euclidean dimensions [11].

The fraction of states below the lower mobility edge is shown in Fig. 18. Again, the behavior is completely

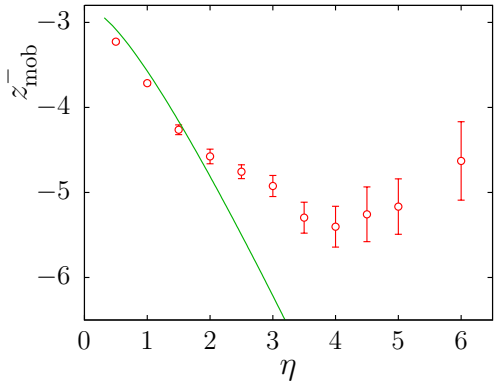

Fig. 17. Position of the mobility edge at the lower tail of the spectrum, for random cubic graph. The solid line is the band edge calculated in EMA.

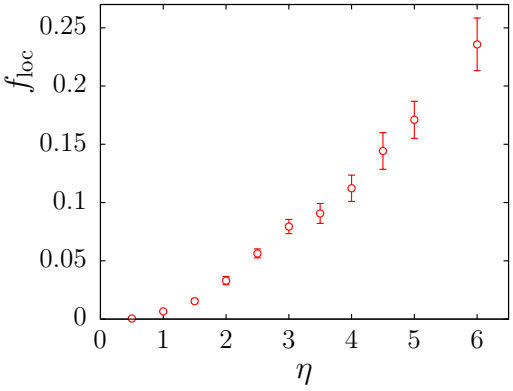

Fig. 18. Dependence of the fraction of states below the lower mobility edge on the strength of the disorder, for random cubic graph. The size is $N = 10^4$.

different from the situation in ER graph. The fraction of localized states is large and grows with the strength of the disorder. We are unable to reach higher disorder strengths η, because establishing the precise value of the mobility edge is increasingly difficult. However, our data are consistent with the claim that beyond a critical strength of disorder the fraction reaches its maximum, i. e. $f_{\rm loc} = 1/2$ for $\eta > \eta_c$.

4.3 IPR distribution

In addition to the dependence of the average IPR on z, we are interested also in the fluctuations of IPR, if we restrict the eigenvalue to a fixed interval $z \in [z_1, z_2]$. Indeed, we found that the fluctuations may be very large, extending up to several orders of magnitude. We show in Fig. 19 a series of histograms for the window $[z_1, z_2]$ sliding from extended states through the transition region, to localized states. As expected, the width of the distribution is largest around the transition, but even in the localized regime it spans about one decade.

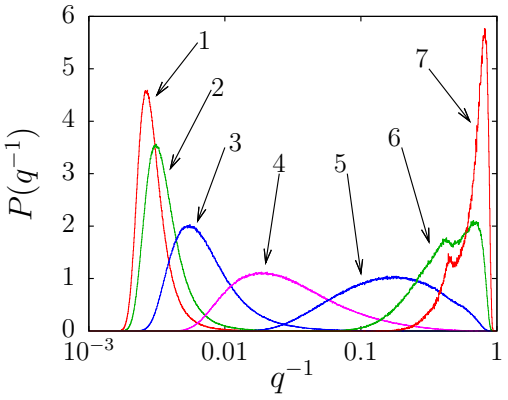

Fig. 19. Histogram of IPR, for states with eigenvalues within a fixed interval, for $\eta = 2$ and $N = 3000$. The arrows point to curves corresponding to intervals $z \in [-0.5, 0.5]$ (line 1), $[-1.5, -0.5]$ (line 2), $[-2.5, -1.5]$ (line 3), $[-3.5, -2.5]$ (line 4), $[-4.5, -3.5]$ (line 5), $[-5.5, -4.5]$ (line 6), and $[-6.5, -5.5]$ (line 7). The data are accumulated from 17000 independent realizations.

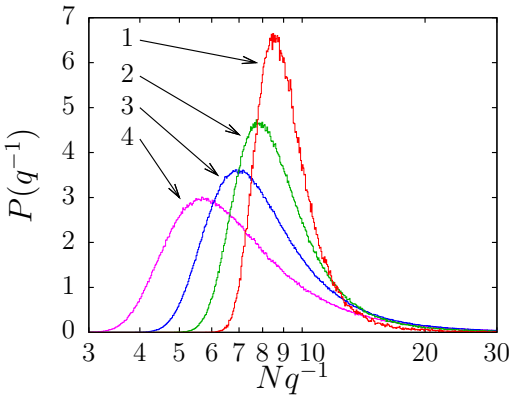

Fig. 20. Histogram of IPR in the range of extended states, $z \in [-0.1, 0.1]$, for $\eta = 2$ and different sizes of the system, $N = 10^4$ (line 1), $N = 3000$ (line 2), $N = 1000$ (line 3), and $N = 300$ (line 4). The data are accumulated from 610, 17000, 130000, and 270000 independent realizations, respectively.

Let us first look at the extended states. The average IPR is expected to scale as $1/N$. Therefore, we plot the histogram against the rescaled value Nq^{-1}, in order to see the convergence for increasing N. Indeed, we can observe in Fig. 20 that the position of the peak approaches to a limit and simultaneously, the width of the peak shrinks. This suggests that in the extended phase, IPR is a self-averaging quantity.

On the contrary, we found that in the localized phase the distribution of IPR is independent of size. Moreover, as the example in Fig. 21 shows, there are non-trivial structures in the distribution. In Fig. 21 we clearly see two distinct peaks and a cusp. Interestingly, the positions of these three structures are slightly below some special values of IPR, namely $q^{-1} = 1$, $q^{-1} = 1/2$, and $q^{-1} = 1/3$. With our data available, we are unable to see further structures

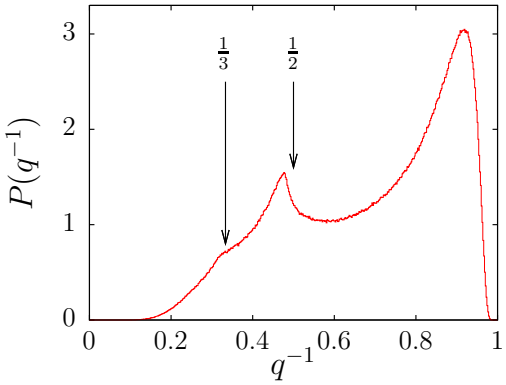

Fig. 21. Histogram of IPR in the range of localized states, $z \in [-8.5, -7.5]$, for $\eta = 5$ and $N = 1000$. The arrows indicate special values if IPR, $q^{-1} = 1/2$ and $q^{-1} = 1/3$. The data are accumulated from 280000 independent realizations.

at $q^{-1} = 1/4$ etc., but we may speculate that they are also present.

Further on, we want to see how these structures evolve when we sweep through the regime of localized states, changing the value of z. We plot in Fig. 22 the series of histograms for $z \in [-8.6 + 0.5n, -8.4 + 0.5n]$, $n = 1, 2, ..., 10$. For large $|z|$, i. e. deep in the localized phase, the peak at $q^{-1} \simeq 1$ dominates, but when we decrease $|z|$, i. e. when we approach the transition, the peak $q^{-1} \simeq 1/2$ takes over, and further on the peak at $q^{-1} \simeq 1/3$ becomes most visible. Simultaneously the peaks broaden and shift to lower values of IPR, so that the structure of distinct peaks is less and less clear.

We can interpret the special positions of the peaks at $q^{-1} = 1$, $q^{-1} = 1/2$, etc. as coming from eigenvectors localized mostly at one, two, etc. sites. In order to support this interpretation, we measured also the weighted average distance between sites. To this end, we first find the shortest paths between each pair of vertices in the current realization of the random cubic graph. Denote $d(i, j)$ the length of this path for vertices i and j. Of course, $d(i, i) = 0$ for every i. Then, for each normalized eigenvector $e_{i\lambda}$ we calculate the weighted average

$$\overline{d}(\lambda) = \frac{\sum_{i,j=1}^{N} d(i,j) e_{i\lambda}^2 e_{j\lambda}^2}{\sum_{i,j=1}^{N} e_{i\lambda}^2 e_{j\lambda}^2} \,. \tag{16}$$

For a vector strictly localized at one single site we get the average distance $\overline{d} = 0$, for a vector localized on a pair of neighbors it is $\overline{d} = 1/2$ and for a vector localized on a pair of sites at distance 2 we have $\overline{d} = 1$. The two latter cases give the same IPR, $q^{-1} = 1/2$, so the average distance brings further information on the eigenvector. We plot in Fig. 21 the joint distribution of IPR and average distance, in the form of two-dimensional histogram. The value of $P(q^{-1}, \overline{d})$ is discriminated by the color, higher values being darker. We clearly observe two black spots corresponding to peaks of the distribution. The first one is located about $q^{-1} \simeq 0.85$ and $\overline{d} \simeq 0.2$, implying states localized around one single site. The shift from the point $q^{-1} = 1$, $\overline{d} = 0$

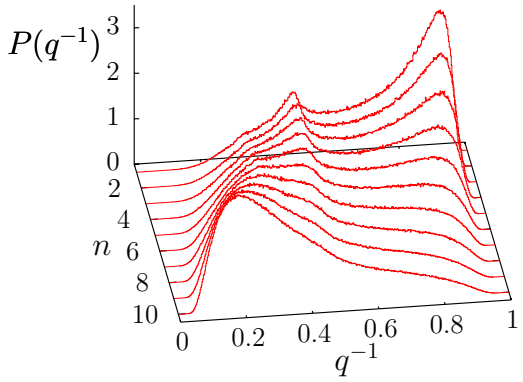

Fig. 22. Series of histograms of IPR in the range of localized states, for $\eta = 5$ and $N = 1000$. The index of the curve n corresponds to the interval of eigenvalues according to the formula $z \in [-8.6 + 0.5n, -8.4 + 0.5n]$. The data are accumulated from 280000 independent realizations.

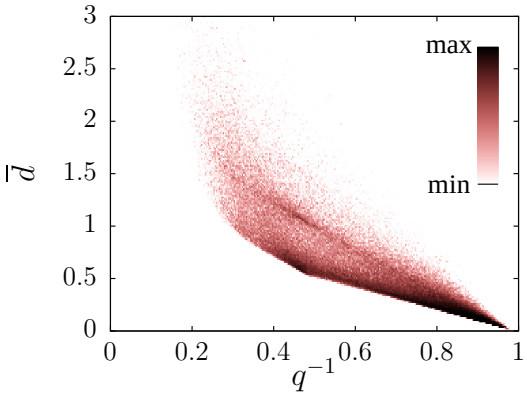

Fig. 23. Two-dimensional histogram of IPR and average distance of sites, in the range of localized states, $z \in [-7.1, -6.9]$, for $\eta = 5$ and $N = 1000$. Darker color indicates higher value of the histogram. The data are accumulated from 30000 independent realizations.

is due to decaying tails of the eigenvector. The second peak is slightly shifted from the ideal position $q^{-1} = 1/2$, $\overline{d} = 1/2$. Clearly, it corresponds to states localized on a pair of neighbors, again with decaying tails. We can also see a darker spot around the position $q^{-1} = 1/2$, $\overline{d} = 1$. This small peak indicates states localized around a pair of sites at distance 2, in. e. on second neighbors.

One might rise a serious suspicion, that each of the peaks in the histogram of IPR corresponds to different realization. If that were true, the multi-peak structure would be the artifact of accumulating data from many independent realizations into one histogram. To check it, we calculated the same histogram for a large system, $N = 30000$. In the localized phase, we found two distinct peaks also in the histogram for one single realization. Moreover, comparing the histograms for a single realization and for 20 independent realizations, we see the same shape of the distribution, within statistical errors. Therefore, the observed peculiarities in the IPR distribution are characteristic of single realizations.

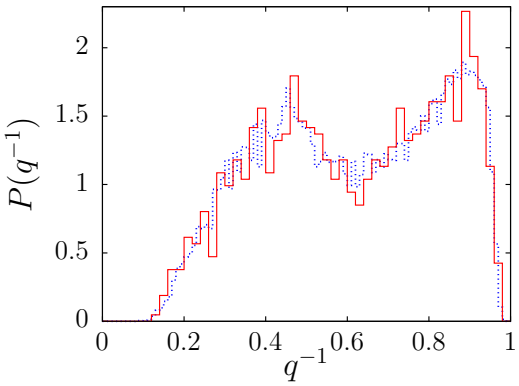

Fig. 24. Histogram of IPR in the range of localized states, $z \in [-7.5, 6.5]$, for $\eta = 6$ and $N = 30000$. The solid line is the histogram for a single realization, while the dotted line is the cumulative histogram for 20 independent realizations.

4.4 Level spacings

An important feature of the localization transition, stressed already in the early works [14,15], is the qualitative change in fluctuations of the imaginary part of the resolvent close to the real axis. It was used for establishing the mobility edge e. g. in Ref. [28]. In fact, this feature is due to the change in level-spacing statistics [46]. Extended states are supposed to obey the level-spacing distribution common to Gaussian orthogonal ensemble (GOE) of random matrices [64], i. e. in a very good approximation

$$P_{\mathrm{GOE}}(x) \propto x \mathrm{e}^{-x^2} \ . \tag{17}$$

(In this expression x is the distance of eigenvalues normalized to the average level spacing). On the other hand, localized states should obey the Poisson statistics

$$P_{\mathrm{Poisson}}(x) \propto \mathrm{e}^{-x} \ . \tag{18}$$

Intuitively, the change in statistics can be understood in terms of level repulsion, which is substantial for extended, but very small for localized states. Therefore, localized states behave as if they were nearly independent and their energies scattered randomly, which gives rise to the Poisson statistics. Because Poisson statistics is characteristic for integrable systems, while statistics like (17) is the fingerprint of a chaotic system, the localization transition can be viewed also as a chaotic-integrable transition.

We analyzed the random cubic graph of size $N = 1000$ and disorder strength $\eta = 2$ and we extracted the level spacing statistics for the spacings between eigenvalues, normalized to the average spacing within certain interval. We used the interval $z \in [-0.1, 0.1]$ as a typical representative of extended states and $z \in [-7, -6]$ as a representative of localized states. The results are shown in Fig. 25. The difference in statistics is clearly visible. The detail in the inset of Fig. 25 shows also that the behavior for small level spacings is close to linear in the extended phase, in accord with Eq. (17). We checked also that the

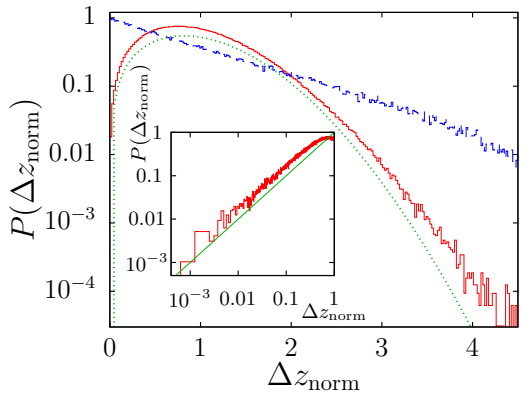

Fig. 25. Distribution of normalized level spacings in the spectrum of random cubic graph with disorder strength $\eta = 2$ and size $N = 1000$. The levels analyzed are restricted to intervals $z \in [-0.1, 0.1]$ (solid line) and $z \in [-7, -6]$ (dashed line). The dotted line is the dependence $\propto \Delta z_{\rm norm} \exp\big(-a(\Delta z_{\rm norm})^2\big)$, with $a = 0.75$, which corresponds to the Gaussian orthogonal ensemble. In the inset we show the detail of the distribution at $z \in [-0.1, 0.1]$ for very small spacings. The straight line is the linear dependence $\propto \Delta z_{\rm norm}$.

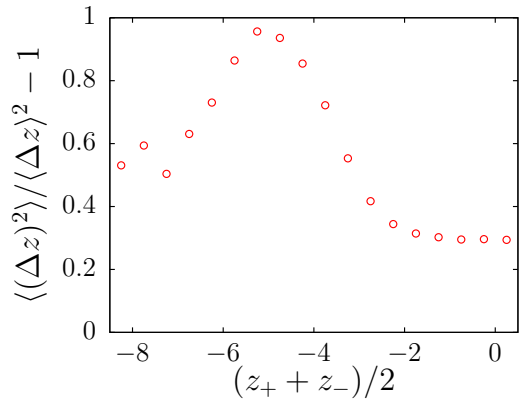

Fig. 26. Relative variance of the level spacing distribution, depending on the center of the interval over which the distribution is calculated. The disorder strength is $\eta = 2$ and the size of the system $N = 1000$.

distribution for localized states decays exponentially, as in Eq. (18). Thus, it is clearly demonstrated that the level spacing statistics gets transformed from from Poisson to GOE when we go from localized to extended regime in the spectrum.

To make this argument quantitative, we calculate the moments of the distribution of level spacings $\langle(\Delta z)^k\rangle = \int (\Delta z)^k\, P(\Delta z) \mathrm{d}\Delta z$ within the interval $z \in [z_-, z_+]$. Then, we plot in Fig. 26 the relative variance of the distribution $\langle(\Delta z)^2\rangle/\langle\Delta z\rangle^2 - 1$. We can clearly see the peak around the transition between localized and delocalized states, marking a qualitative change in the level spacing distribution.

5 Conclusions

Numerically diagonalizing matrices up to size 10000 × 10000, we investigated localization transition in Erdős-Rényi and random cubic graphs. In ER graphs, the free parameter was the average degree, while in random cubic graphs, the parameter was the strength of disorder in the diagonal matrix elements. The quantity to discriminate between localized and extended regimes was the inverse participation ratio. We averaged IPR over large number of realizations and using finite-size scaling, we extracted the mobility edge. The benchmark for the position of the mobility edge was the band edge found in the effective medium approximation.

The localization properties in ER and random cubic graphs are much different. In the former, the mobility edge goes more or less in parallel with the EMA band edge, when we change the average degree, and the fraction of localized states decreases when the average degree grows. In the latter, the EMA band edge is significantly farther than the mobility edge, or else, much of the localized states are actually present within the range of EMA spectrum. The results are consistent with analytical findings which predicted that a critical disorder strength exists, beyond which all states are localized.

The inverse participation ratio exhibits rather strong fluctuations. In the extended phase, the relative width of the IPR distribution decreases with increasing system size, while in the localized phase the width of the distribution approaches a finite value. Moreover, the distribution contains non-trivial structures of several peaks. We interpret these structures as corresponding to states localized around one, two, three, etc. sites.

For the random cubic graphs, we analyzed also the level spacing statistics confirming the expectation that in the localized region the statistics is close to Poissonian, while in the extended region it is close to the statistics of Gaussian orthogonal ensemble.

I wish to thank to J. Mašek for numerous useful comments. This work was carried out within the project AV0Z10100520 of the Academy of Sciences of the Czech Republic and was supported by the MŠMT of the Czech Republic, grant no. OC09078.

References

1. P. W. Anderson, Phys. Rev. **109**, 1492 (1958).
2. E. Abrahams (Ed.), *50 Years of Anderson Localization* (World Scientific, Singapore, 2010).
3. P. A. Lee and T. V. Ramakrishnan, Rev. Mod. Phys. **57**, 287 (1985).
4. B. Kramer and A. MacKinnon, Rep. Prog. Phys. **56**, 1469 (1993).
5. F. Evers and A. D. Mirlin, Rev. Mod. Phys. **80**, 1355 (2008).
6. R. del Rio, S. Jitomirskaya, Y. Last, and B. Simon, Phys. Rev. Lett. **75**, 117 (1995).

7. E. Abrahams, P. W. Anderson, D. C. Licciardello, and T. V. Ramakrishnan, Phys. Rev. Lett. **42**, 673 (1979).
8. D. Vollhardt and P. Wölfle, Phys. Rev. B **22**, 4666 (1980).
9. D. Vollhardt and P. Wölfle, in: *Electronic Phase Transitions*, eds. W. Hanke and Ya. V. Kopaev p. 1 (North-Holland, Amsterdam, 1992).
10. I. M. Suslov, Sov. Phys. JETP **81**, 925 (1995).
11. V. Janiš and J. Kolorenč, Phys. Rev. B **71**, 033103 (2005).
12. F. J. Wegner, Phys. Rev. B **19**, 783 (1979).
13. K. B. Efetov, Adv. Phys. **32**, 53 (1983).
14. R. Abou-Chacra, P. W. Anderson, and D. J. Thouless, J. Phys. C: Solid State Phys. **6**, 1734 (1973).
15. R. Abou-Chacra and D. J. Thouless, J. Phys. C: Solid State Phys. **7**, 65 (1974).
16. D. E. Logan and P. G. Wolynes, Phys. Rev. B **31**, 2437 (1985).
17. P. D. Antoniou and E. N. Economou, Phys. Rev. B **16**, 3768 (1977).
18. S. M. Girvin and M. Jonson, Phys. Rev. B **22**, 3583 (1980).
19. K. B. Efetov, Physica A **167**, 119 (1990).
20. A. D. Mirlin and Y. V. Fyodorov, Nucl. Phys. B **366**, 507 (1991).
21. H. Kunz and B. Souillard, J. Physique Letters **44**, L-411 (1983).
22. P. Stollmann, *Caught by disorder. Bound states in Random Media* (Birkhäuser, Boston, 2001).
23. M. Aizenman and S. Warzel, Phys. Rev. Lett. **106**, 136804 (2011).
24. P. Markoš, Acta Physica Slovaca **56**, 561 (2006).
25. C. Monthus and T. Garel, Phys. Rev. B **81**, 224208 (2010).
26. P. Cizeau and J.-P. Bouchaud, Phys. Rev. E **50**, 1810 (1994).
27. A. Cavagna, I. Giardina, and G. Parisi, Phys. Rev. Lett. **83**, 108 (1999).
28. S. Ciliberti, T. S. Grigera, V. Martín-Mayor, G. Parisi, and P. Verrocchio, Phys. Rev. B **71**, 153104 (2005).
29. R. Kühn, J. Phys. A: Math. Theor. **41**, 295002 (2008).
30. F. L. Metz, I. Neri, and D. Bollé, Phys. Rev. E **82**, 031135 (2010).
31. G. Biroli, G. Semerjian, and M. Tarzia, Prog. Theor. Phys Suppl. **184**, 187 (2010).
32. C. Monthus and T. Garel, J. Phys. A: Math. Theor. **44**, 145001 (2011).
33. F. R. K. Chung, *Spectral Graph Theory*, (American Mathematical Society, 1997).
34. B. Bollobás, *Random Graphs* (Academic Press, London, 1985).
35. G. J. Rodgers and A. J. Bray, Phys. Rev. B **37**, 3557 (1988).
36. G. J. Rodgers and C. De Dominicis, J. Phys. A: Math. Gen. **23**, 1567 (1990).
37. Y. V. Fyodorov and A. D. Mirlin, J. Phys. A: Math. Gen. **24**, 2219 (1991).
38. Y. V. Fyodorov and A. D. Mirlin, Phys. Rev. Lett. **67**, 2049 (1991).
39. A. Khorunzhy and G. J. Rodgers, J. Math. Phys. **38**, 3300 (1997).
40. G. Biroli and R. Monasson, J. Phys. A: Math. Gen. **32**, L255 (1999).
41. M. Bauer and O. Golinelli, J. Stat. Phys. **103**, 301 (2001).
42. G. Semerjian and L. F. Cugliandolo, J. Phys. A: Math. Gen. **35**, 4837 (2002).
43. T. Rogers, I. Pérez Castillo, R. Kühn, and K. Takeda, Phys. Rev. E **78**, 031116 (2008).
44. S. N. Evangelou, Phys. Rev. B **27**, 1397 (1983).
45. S. N. Evangelou, J. Stat. Phys. **69**, 361 (1992).
46. S. N. Evangelou and E. N. Economou, Phys. Rev. Lett. **68**, 361 (1992).
47. S. N. Dorogovtsev, A. V. Goltsev, J. F. F. Mendes, and A. N. Samukhin, Phys. Rev. E **68**, 046109 (2003).
48. M. Sade, T. Kalisky, S. Havlin, and R. Berkovits, Phys. Rev. E **72**, 066123 (2005).
49. A. L. Cardoso, R. F. S. Andrade, and A. M. C. Souza, Phys. Rev. B **78**, 214202 (2008).
50. G. Zhu, H. Yang, C. Yin, and B. Li, Phys. Rev. E **77**, 066113 (2008).
51. S. Jalan, N. Solymosi, G. Vattay, and B. Li, Phys. Rev. E **81**, 046118 (2010).
52. O. Giraud, B. Georgeot, and D. L. Shepelyansky, Phys. Rev. E **80**, 026107 (2009).
53. F. Slanina and Z. Konopásek, Adv. Compl. Syst. **13**, 699 (2010).
54. C. Bordenave and M. Lelarge, arXiv:0801.0155 (2008).
55. F. Slanina, Phys. Rev. E **83**, 011118 (2011).
56. E. N. Economou and M. H. Cohen, Phys. Rev. B **5**, 2931 (1972).
57. R. Kühn and J. van Mourik, J. Phys. A: Math. Theor. **44**, 165205 (2011).
58. Z. Burda, J. Duda, J. M. Luck, and B. Waclaw, Phys. Rev. Lett. **102**, 160602 (2009).
59. F. Delyon, B. Simon, and B. Souillard, Phys. Rev. Lett. **52**, 2187 (1984).
60. F. Delyon, B. Simon, and B. Souillard, Ann. Inst. H Poincaré, Phys. Theor. **42**, 1985 ().
61. Y. V. Fyodorov, A. D. Mirlin, and H.-J. Sommers, J. Phys. I France **2**, 1571 (1992).
62. M. Kolář and F. Slanina, Eur. Phys. J. B **31**, 379 (2003).
63. L. Erdős, A. Knowles, H.-T. Yau, and J. Yin, arXiv:1103.1919 (2011).
64. M. L. Mehta, *Random matrices* (Academic Press, San Diego, 1991).